A Miniaturized Electromagnetic Generator With Planar Coils and Its Energy Harvest Circuit

Lun-De Liao[1], Paul C.-P. Chao[1,2], Jian-Ting Chen[1], Wei-Dar Chen[1], Wei-Hsuan Hsu[1], Chi-Wei Chiu[1], and Chin-Teng Lin[1], *Fellow, IEEE*

[1]Department of Electrical and Control Engineering, National Chiao Tung University, Hsinchu 300, Taiwan
[2]Institute of Imaging and Biophotonics, National Chiao Tung University, Hsinchu 300, Taiwan

This study presents design, analysis and experiment of a miniaturized rotary generator in size of $10 \times 10 \times 2$ mm^3 and its compact energy harvest circuit chip. The designed generator consists of patterned planar copper coils and a multipolar hard magnet ring made of NdFeB. To perform modeling, a harmonic-like magnetic field model along the circumferential path of each magnetic pole is assumed with the assistance from measured peak magnetic flux densities. This is followed by the application of Faraday's law to predict generated electromotive forces (EMFs) in terms of the relative rotational speed between the magnet ring and coils. The genetic algorithm (GA) is next applied to optimize the critical dimensions of the miniaturized generator. The theoretical model of this power microgenerator is evaluated and compared with experimental results, and it is found that the analytical simulation shows a good agreement with the experimental results. The optimized generator offers 4.5 V and 7.23 mW in root mean square (rms) at 10 000 r/min. With microgenerator successfully fabricated, a novel energy harvest circuit employing Dickson charge pump is designed and fabricated via the 0.35-um process offered by National Chip Implementation Center (CIC) of Taiwan. This charge pump circuit owns the merit of almost-zero thresholds of employed metal–oxide–semiconductor (MOS) transistors, enabling the conversion of low-power alternating current (ac) signals by the microgenerator to direct current (dc) ones.

Index Terms—**Electromotive forces (EMFs), energy harvest circuit, miniaturized rotary generator, self-power system.**

I. Introduction

MINIATURIZED or microgenerators have been promising devices for high-density power conversion in portable electronics, robotics, and various other microsystem applications. This generator is capable of serving as a transducer in a self-power system to scavenge energy from translational or rotational vibrations [1], [2]. The obtained power could be applied to a rotor balancing ring [3], or to the pervasive networks of wireless sensor and communication nodes [4], [5]. Recent studies have reported two different types of power generation: electromagnetic and piezoelectric ones. They are capable of generating powers of 0.53 mW at 322 Hz, and 3 μW at 90 Hz, respectively [1]. Therefore, the electromagnetic microgenerators demonstrated their superiority in terms of high-power generation over piezoelectric microgenerators [6].

With the aim to render high-power density acquisition, some studies were focused on "rotary" electromagnetic microgenerators, which were initiated by Das *et al.* [7], who presented a permanent magnet generator for microscale systems, which is capable of generating 2.5 W. Arnold *et al.* [8]–[10] presented a theoretical modeling for the optimization of a microscale, axial-flux, permanent-magnet generator. Holmes *et al.* [11] reported an axial-flux permanent magnet electromagnetic generator with a diameter of 7.5 mm tested and shown to deliver an output power of 1.1 mW per stator at a rotation speed of 30 000 r/min. Raisigel *et al.* [12], [13] reported a planar generator with a diameter of 8 mm. The first prototype of a microturbo generator driven by compressed air delivered an electric output power of 14.6 mW at 58 000 r/min. As to the rear-end energy harvest via the charge pump, it is known that the classical charge pump was first proposed by Dickson [14], which is based on a diode-connected metal–oxide–semiconductor (MOS) as charge transfer device. Tanzawa and Tomoharu [15] presented a complete analysis on the dynamics of this Dickson charge pump. Starzyk *et al.* [16] later developed another charge pump circuit similar to Dickson's in [14].

This paper presents the design, manufacture and analysis of a new miniaturized rotary electromagnetic microgenerator. Different from the previous studies, the genetic algorithm (GA) [17] is utilized to optimize the critical parameters of the microgenerator, which directly influences the electrical output power. In addition, also presented is a highly efficient energy harvesting circuit employing Dickson charge pump [14], which is implemented via the 0.35-um complementary MOS (CMOS) process.

The generator development process includes the following steps. First, different patterns of Cu planar microcoils are manufactured using the filament winding method. Second, the multipolar NdFeB magnets that provide the external field are made of raw powder materials by molding, sintering, heat treatment, and anisotropic magnetization. Third, the microcoil and multipolar magnet are assembled together. With manufacturing capability, the GA [17] is utilized to optimize the critical parameters of the microgenerator—the width and span of the coils in the microgenerator. The optimization is based on the assumption of a harmonic magnetic field density induced by the rotor magnets, as opposed to all previous studies, where either a complicated magnetic field [10]–[12] or an unrealistic uniform field [13] was assumed. This simple assumption makes possible the ensuing GA optimization on the critical sizes of the miniaturized generator.

As to the energy harvest circuit, it is well known that a well-designed Dickson's charge pump provides approximately an output voltage: $V_{\mathrm{OUT}} = N \cdot (V_{DD} - V_T)$ where N is the number of stages, V_{DD} is the supply voltage, and V_T is the

Manuscript received March 06, 2009. Current version published September 18, 2009. Corresponding author: P. C.-P. Chao (e-mail: pchao@mail.nctu.edu.tw).

Color versions of one or more of the figures in this paper are available online at http://ieeexplore.ieee.org.

Digital Object Identifier 10.1109/TMAG.2009.2023999

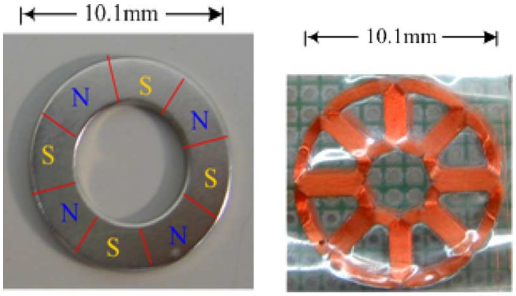

Fig. 1. (a) The magnet ring of NdFeB as a rotor. (b) The fabricated miniaturized planar coils as a stator.

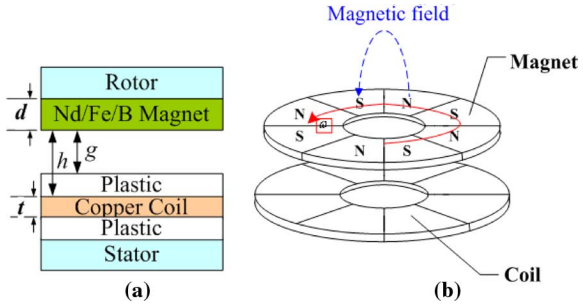

Fig. 2. (a) Internal structure and materials of the generator. (b) A 3-D schematic of the miniaturized generator.

threshold voltage of the diode connected MOS transistors used in the circuit. Unfortunately, as the voltage is increased by charge pumping, the threshold voltage of the MOS transistors increases due to the body effect, the voltage step $V_{DD} - V_T$ of each stage is reduced, and the overall efficiency decreases. The proposed energy-harvest charge pump circuit, playing the role of alternating current/direct current (ac–dc) converter, employs a series of diode-connected MOS transistors. The gates and drains of these transistors are connected with predesigned capacitances, which are able to store desired voltage differences to reduce the threshold voltages of the MOS diodes. In this way, the output voltage $V_{\rm OUT}$ is increased to its possible extreme, maximizing the output power of the designed energy harvest circuit. This charge pump circuit owns the merit of almost-zero thresholds for the employed MOS transistors, thus enabling low-power ac signals by the microgenerator to be converted to dc ones.

II. Miniaturized Rotary Generator Design and Fabrication

The designed miniaturized rotary generator consists of patterned planar copper coils and a multipolar hard magnet ring made of NdFeB. They are photographed as shown in Fig. 1(a) and (b), respectively. It is seen from this figure that eight coils are fabricated, and the pattern of each coils is designed as sector-shape loops. Eight coils correspond to eight S and N poles in sectoral shapes, which are realized by a magnetized segments of NdFeB embedded in a rotating rotor ring.

The schematic illustration of the entire generator system is presented in Fig. 2(a) and (b), where Fig. 2(a) presents a cross-section view that elaborates the internal material and structure, while Fig. 2(b) is a simple 3-D schematic of the generator. In Fig. 2(a), the lower component plays the role of a stator, which is composed of copper miniaturized coils and plastic films to protect the coils. The upper component shaped as a ring plays the role of a rotor, which is composed of the eight-pole NdFeB magnet ring. The thickness of copper coil is denoted by t and the thickness of the NdFeB magnet d. It is noted that the thickness of plastic film is very thin as compared to t such that it can be neglected in simulation process. The gap between the layer of the stator of copper coils and the rotor of NdFeB magnet is denoted by g.

The multipolar magnet ring of NdFeB is composed of four interplaced S- and N-pole sectoral segments. The sintering technology is used to manufacture eight-pole magnets, and the custom-designed stator is used to magnetize the NdFeB magnet, as shown in Fig. 1(a). Measurements using a vibrating magnetometer are conducted to obtain the B–H curve of the sintered magnets of NdFeB. A satisfactory performance of a hard magnet is rendered with a residual induction (Br) of 1.1 T and a coercive force (Hc) of 910 kAm^{-1}.

On the other hand, the method of filament winding is adopted to manufacture the coils for fast prototyping. This filament winding equipment requires precise x–y positioning tables and z-axis height controlling systems. Eight planar coils with a single filament of copper wire are successfully manufactured, shown in Fig. 1(b). Using the filament winding method, a precise geometric pattern of coils is impregnated on the 50-μm-thick polyethylene terephthalate (PET) substrate prepared for use in this study. The use of the flexible PET substrate enables folding and stacking, and thus multiple layers of coils. The resistivity of the copper planar miniaturized coils is $1.7 \times 10^{-8}\ \Omega/\mathrm{m}$.

III. Theoretical and Numerical Analysis

With the basic structure of the miniaturized generator determined in Section II, the theoretical modeling assisted with finite-element simulation via software ANSYS is performed in this section. This aims to predict induced voltage and resulted power. Having the predicted voltage in hands, the optimization is executed in Section IV for optimal size of the coils and magnet.

The theoretical modeling starts with considering one single coil sector, as shown in Fig. 3, where the four vertices are denoted as abcd. The distance between the internal edge of the coil sector and the stator center, the radial coil sector span, and the coil width are denoted, respectively, as r, b, and w. In the operations with the ring-shaped magnet rotor, each sectoral coil loop will face each of eight magnetized poles of NdFeB embedded in the rotor ring. As the rotor is in a rotational speed ω, as shown in Fig. 2(b), the induced magnetic flux cross the segments of ab and cd, thus, inducing electromotive force (EMF) voltages, while the directions of segments bc and da are parallel to the flux, generating no voltage. Based on Fleming's right-hand side rule, the induced current by segment ab flows from point b to a, while the current by segment cd flows from d to c.

With physical ground understood, the next task is to compute the EMF voltage induced by the crossing of magnetic flux over the coils. The computation starts with considering a pair

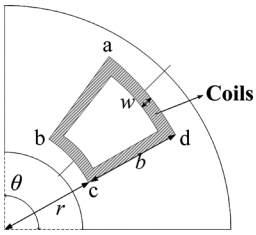

Fig. 3. Dimensions of one single sectoral coil loop in the stator.

of N and S magnetic poles and one coil sector, as schematically shown in Fig. 4, where the magnetic flux starting from N-pole to S-pole clearly cross the coils. As the magnet poles are moving horizontally, based on the well-known Faraday's law, the induced EMF voltage $V_{\rm emf}$ is equal to the change rate of total magnetic flux ϕ over a region enclosed by the coil loop sector; therefore

$$V_{\rm emf}(t) = -\frac{d\phi}{dt} = -\frac{d}{dt}\int_s B(\theta)\cdot dA = -\int_s \frac{\partial B(\theta)}{\partial t}\cdot dA \quad (1)$$

where $B(\theta)$ is the magnetic flux density along the circumferential direction of the rotor ring and coils. Assuming the change of the magnetic flux density from N-pole to S-pole along the local circumferential direction θ horizontally is like a sum of a harmonic function and a nonzero averaged density, the magnetic flux across one single loop coil is

$$B(\theta) = \bar{B}\cos\theta + B_0 \quad (2)$$

where $\overline{B}$ is the magnitude of the flux density variation over one single coil loop, while B_0 is the averaged density. Incorporating (2) into (1) and assuming the magnet rotor is in a constant rotational speed, i.e., $\theta = \omega t$, the induced EMF voltage by one single coil sector can be obtained as

$$V_{\rm emf}(t) = -\frac{d\phi(t)}{dt} = \frac{4}{P}\omega\bar{B}A\sin\omega t \quad (3)$$

where A is the area enclosed by a single coil loop, and P is the number of poles in the miniaturized generator. Considering the eight-pole magnet rotor in this study, i.e., $P = 8$, and multiple planar loops for one single sectoral coil, the net induced EMF voltage induced by the entire generator becomes

$$V_{\rm emf}(t) = -\frac{d\phi(t)}{dt} = 4\omega\bar{B}\left(\sum_{i=1}^{n} A_i\right)\sin\omega t \quad (4)$$

where A_i is the enclosed area of the ith coil loop in a sector, and n is the number of coil turns for a sector. Assuming the coil width w as shown in Fig. 3 is small, each coil loop has the same shape and size. Thus, (4) becomes

$$V_{\rm emf}(t) = -\frac{d\phi(t)}{dt} = 4n\omega\bar{B}A\sin\omega t. \quad (5)$$

With measured $\overline{B}$, the maximum value of the magnetic flux density along θ, the induced EMF voltage can be estimated by the above equation. The magnitude of the induced EMF is thus $4n\omega\overline{B}A$.

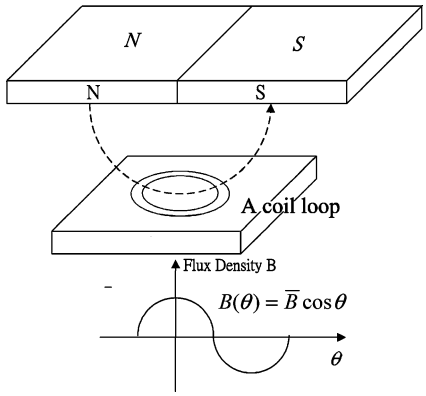

Fig. 4. Illustration of magnetic flux and its density change along θ.

In addition to the afore-derived equations for predicting the induced EMF, the finite-element modeling and analysis via software ANSYS is conducted, where the properties of the sintered NdFeB magnet, previously mentioned in Section II, are adopted. Fig. 5(a) and (b) shows the simulated magnetic flux for a single pair of poles and the perpendicular (z-direction) component of the flux density along θ and at a distance h from the surface of the coils ($h = 0.9$ mm), respectively. The resulted flux density in Fig. 5(b) appears close to a harmonic function plus a constant average, validating the assumption in (2). Note that the slight jaggedness around the peaks of the density curves in Fig. 5(b) resulted from limited number of the grid mesh density assumed in ANSYS simulation. In Fig. 5(b), a maximum density of 1.05 T results, which is close to the density measured by a Gaussian meter in the laboratory. Finally, $\overline{B} = 0.13$ T validated from Fig. 5(b) would be used for $\overline{B}$ in (5) for theoretical predictions for GA optimization in Section IV.

IV. GA Optimization

With valid prediction models in hands, optimization is next performed to determine critical dimensions of the miniaturized generator. This optimization process consists of two steps: problem formulation and the employment of GA. The formulation starts with defining the output power of the generator as the fitness function to maximize, with the aim to increase the power of generator as large as possible. The output power is the ratio of root mean square (rms) of induced EMF voltage, $V_{\rm emf}$, over the net coil resistance of the generator $R_{\rm coil}$; thus

$$P = \frac{V_{\rm rms}^2}{2R_{\rm coil}} \quad (6)$$

where $V_{\rm rms}$ can be calculated by the previously derived (5), or more precisely, based on the nonuniform magnetic field strength simulated by ANSYS for the magnets in the rotor ring. On the other hand, the net coil resistance $R_{\rm coil}$ is computed based on its proportionality to the total length of the coils, which is in fact

$$R_{\rm coil} = \frac{\rho L}{\hat{A}} = \frac{\rho n}{\hat{A}}(4\pi r + 16b) \quad (7)$$

where L is the coil length, $\hat{A}$ is the cross section of the coil, ρ is the copper resistance per unit volume, n is the number of turns for a single coil sector, and r and b are previously defined, as

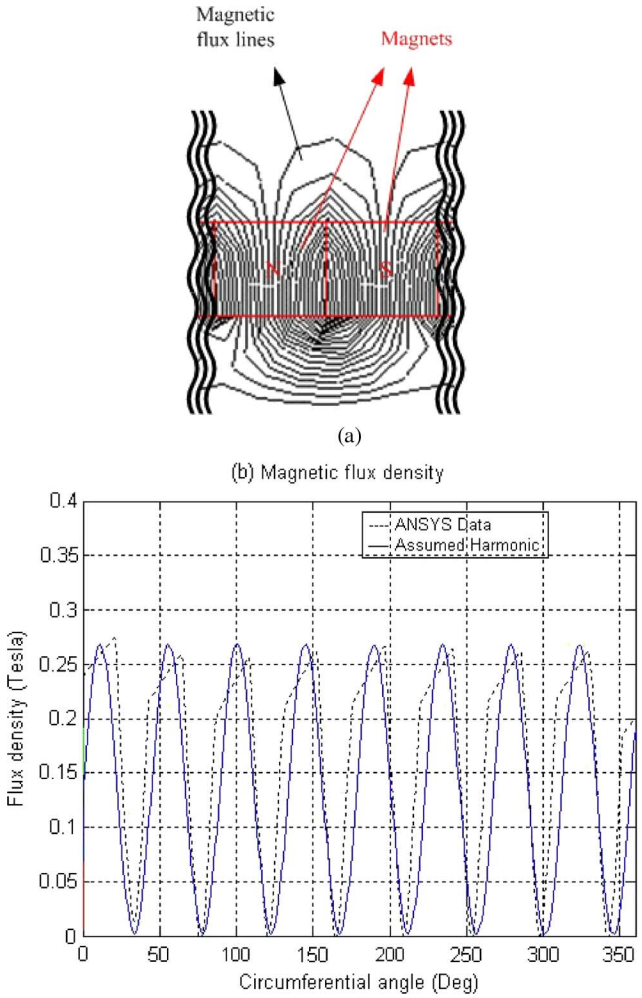

Fig. 5. (a) Simulated magnetic flux distribution for a pair of poles. (b) Flux density along θ by ANSYS.

shown in Fig. 3. Note that (7) assumes the same size for each coil loop and eight sectoral coils. This modeling limitation can be easily released by modifying (7) based on the diameter of the coil. The details of modification on (7) are not presented herein for the sake of simplicity. On the other hand, in (7), the copper resistance per unit length, i.e., $\rho/\hat{A}$, is 5.7 $\times 10^7$ Ω/m. Considering the coil resistance in (7), the induced EMF voltage derived from (5) and the nonuniform magnetic field strength resulted from the finite-element analysis via ANSYS, the power can be computed, which is defined as the fitness function to be maximized by GA.

With the computation procedure established for the fitness function, the next step of optimization is to choose the least number of independent component dimensions possible as the design variables for optimization and also determine their constraints. To this end, it is assumed prior to optimization that 1) there are eight coil sectors containing multiple turns of coils and corresponding to eight poles embedded in the magnet rotor; and 2) the outer dimensions of the stator and rotor are fixed. A thorough investigation leads to that, with the coil diameter fixed, two independent design variables are chosen as the radial coil span b and the coil width w, as defined in Fig. 3. Their constraints are set up as 5% variation of their nominal values.

GA [17] is applied to find the optima of the predefined design variables. The GA process starts with representing the value of each design variable by an array of eight binary bits, and having population of 50 or 100 to enable crossover operations and mutations between generations. Different populations are chosen to observe its effects on GA optimization. The crossover and mutation rates are set as 0.9 and 0.4, respectively. The maximum number of generation for evolution is set as 10 000 initially and is then decreased to the required for computation efficiency. A number of optimization results show a consistent convergence in the optima within preset maximum number of generations, confirming that the optimization results are truly optima. Furthermore, the optima obtained by varied GA trials lead to almost the same optimum power 7.05 mW in rms and the corresponding optimal values of design variables, which are $b =$ 2.8 mm and $w = 1.7$ mm. The optimization results reveal that the coils should not fully fill available sectoral space to render the maximum power. It is due to the fact that long coils lead to large resistance and then decreasing the power. Note also that although the number of design parameters to be optimized by GA herein is only two, where a complicated method technique like GA may be necessary, the proposed GA technique can be easily extended to a case considering more design variables.

V. Design of Energy Harvesting Circuit

The Dickson charge pump [14] with its improvement is utilized in this study to harvest the electrical power generated by the microgenerator. For valid operation of the Dickson charge pump, the diode-connected MOS transistors normally pose threshold voltages about 0.6 V. The input voltage from the microgenerator must overcome this relatively high threshold to charge energy-collecting capacitors, therefore, lowering the power-collection efficiency. To remedy the problem, a novel energy harvest circuit is proposed in this study, which designs and imposes capacitances across gates and drains of MOS transistors in order to store desired voltage differences to reduce the threshold voltages of the MOS diodes. In this way, the output voltage is increased to its possible extreme, maximizing the output power of the designed energy harvest circuit.

The design principle of the aforementioned energy harvest circuit is elaborated in details, which starts with the proposed diode-connected MOS transistor, shown in Fig. 6(a) and (b). Fig. 6(a) illustrates the operation with switch (SW) on, while Fig. 6(b) does it with the switch off. When M1 SW is on, it stores the voltage V_1 equal to V_T (threshold voltage of the MOS transistor) in the capacity C_1. When M1 switch is turned off, the MOS diode owns zero threshold voltage as $V_G = V_D + V_T$, as shown in Fig. 6(b). The aforementioned scenario is nonetheless an ideal case. With inevitable imprecise control of M1 SW, C_1 is charged overtime, resulting in a slight increase in the voltage across C_1, as shown in Fig. 6(c). In this figure, the increasing slope is slower in the overcharge period than the normal charging one, due to the fact that an M5 induces an additional branch current i_5.

The successfully designed diode-connected MOS transistors with zero threshold voltage are employed next to forge the entire Dickson charge pump circuit as shown in Fig. 7(a). The operation process of this designed charge pump circuit includes two different steps. Step 1 is to charge $\{C_1, \ldots, C_4\}$ in the circuit in a series connection, along with $\{C_5, \ldots, C_8\}$ charged at the

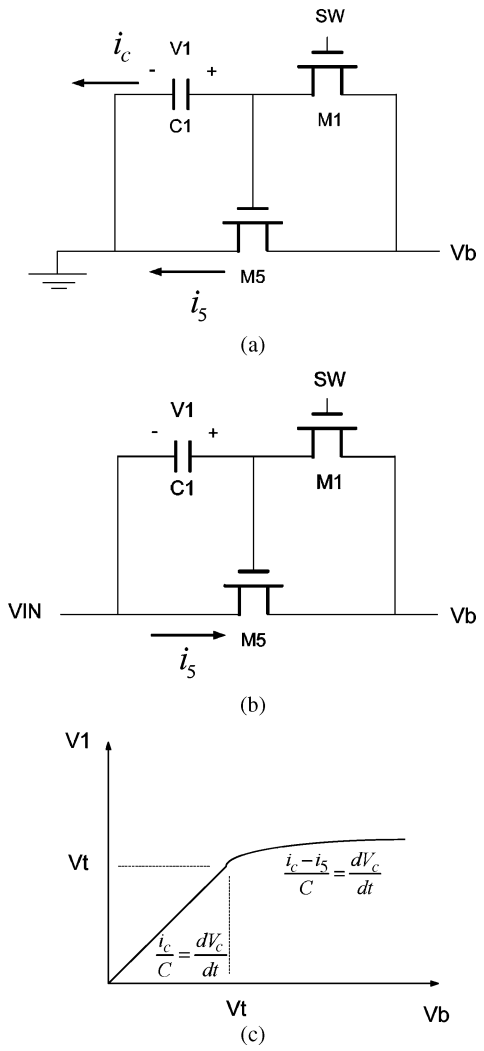

Fig. 6. A single diode-connected MOS transistor with (a) SW on, (b) SW off, and (c) the charge curve of V_1 versus bias V_b.

same time. Based on basic voltage division, it can be derived at steady state that

$$V_1 = \frac{C_2}{C_1 + C_2 + C_5} V_6 \tag{8a}$$

$$V_2 = \frac{C_3}{C_3 + [(C_1 + C_5) \| C_2 + C_6]} V_7 \tag{8b}$$

$$V_3 = \frac{C_4}{C_4 + [(C_1 + C_5) \| C_2 + C_6] \| C_3 + C_7} V_b \tag{8c}$$

$$V_4 = V_b - V_1 - V_2 - V_3. \tag{8d}$$

With (8)–(11) in hands, V_b and $\{C_1, \ldots, C_4\}$ are designed to render $\{V_1, \ldots, V_4\}$ as almost equal to the threshold of MOS transistor individually. Step 2 of the operation is to switch off $\{M1, \ldots, M4\}$ and then allow the output power from the generator to charge C_5 to C_8, yielding

$$\begin{aligned} V_5 &= V_{\text{in}} - V_T + V_1 \\ V_6 &= V_{\text{in}} + V_5 - V_T + V_2 \\ V_7 &= V_{\text{in}} + V_6 - V_T + V_3 \\ V_8 &= V_{\text{out}} = V_{\text{in}} + V_7 - V_T + V_4. \end{aligned} \tag{9}$$

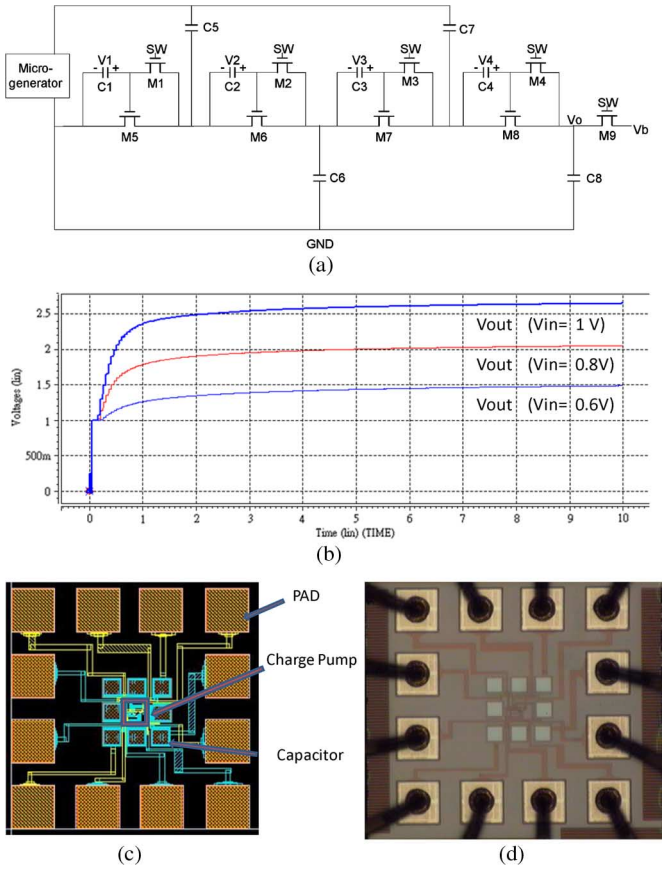

Fig. 7. (a) Energy harvest circuit, (b) simulation, (c) chip layout, and (d) microphoto of fabricated IC.

Combining all the above equations yields

$$V_{\text{out}} = 4V_{\text{in}} - 4V_T + V_1 + V_2 + V_3 + V_4. \tag{10}$$

Reminding that in the first step, it is achieved that $V_T \approx V_i$, $i = 1, \ldots, 4$

$$V_{\text{out}} \approx 4V_{\text{in}} \tag{11}$$

which is stored in the overall output capacitor C_8. However, due to the facts that 1) V_b may not be precisely designated to their desired values and 2) the switching of the diode-connected MOS transistor is not right on time, the output voltage is normally substantially below $4V_{\text{in}}$.

With the energy harvest circuit successfully designed, the electrical dynamics of this circuit is simulated using HSPICE, as shown in Fig. 7(b). It is seen from this figure that the output voltage reaches a steady voltage, which is ready to be used for subsequent applications. On the other hand, the very large scale integration (VLSI) layout of this circuit is constructed by CADENCE, as shown in Fig. 7(c) using TSMC 0.35-um CMOS process. Finally, the designed circuit is fabricated via the TSMC 0.35-um process offered by National Chip Implementation Center (CIC) of Taiwan, the microphoto of which is shown in Fig. 7(d). The resulted core area of the circuit of the IC chip is 0.4 mm $\times$ 0.4 mm as shown in Fig. 7(c) and (d). It has eight pin pads that include those for supply voltage (1.5 V), ground, input, output, and the low-pass filter.

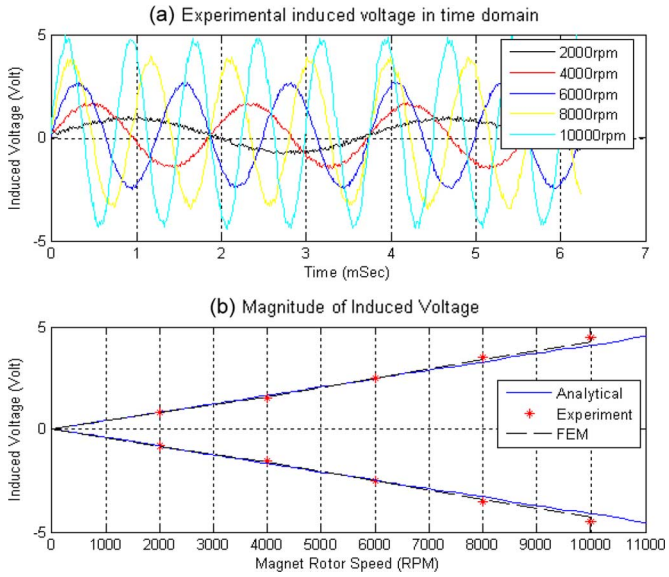

Fig. 8. (a) Experimental induced voltage in time domain. (b) Induced voltage amplitude for varied speeds.

VI. Experimental Validation

The miniaturized generator with optimized critical dimensions obtained in Section V is fabricated for experimental validation. First, the magnet is fixed on a rotary mechanism and the microcoil is attached on a static platform. The gap between microcoils and magnet is set at 1 mm. Second, the rotary mechanism is driven by power supply to make the multipolar magnet rotate at different angular velocity or frequency. When the eight-polar magnet is rotated relative to Cu microcoil, the planar microcoil induces voltage and current. In experimental procedure, the eight-pole magnet rotor disk is fixed to a rotor shaft and the copper planar coils are placed horizontally and facing the magnet rotor rings with a gap of 0.8 mm. The rotor shaft is driven by an electric motor for different rotating speeds. When the magnet rotor is rotated in a specific speed, the relative motion between the coils and eight-pole magnets induces nonzero currents in the coils and results in EMF voltages.

The induced voltage with respect to time is measured for different rotational speeds, with a resistive load matching the coil resistance of 1.4 kΩ. These measured voltages are shown in Fig. 8(a), where sinusoidal voltage outputs are present. This is due to the fact that the magnetic field generated by the eight-pole magnet rotor is a harmonic-like function. It is also seen from this figure that with higher rotational speed, the magnitude of the induced voltage is increased. On the other hand, Fig. 8(b) presents magnitudes of the induced voltage versus speed. The relationship between the voltage magnitude and the rotor speed appears to be almost linear, validating the effectiveness of (5). Also depicted in Fig. 8(b) are theoretical (analytical) predictions for the EMF voltage based on (5) and finite-element method (FEM) results by ANSYS. Only a slight difference is seen among the theoretical, FEM, and experimental voltages at different speeds. It confirms that the established theoretical and FEM model is effective to offer correct predictions on the generator performance and used for optimization in the previous section. It can be deducted from the results in Fig. 8(b) that the optimized generator induces a realistic peak voltage of 4.5 V at 10 000 r/min. The generator offers a maximum power output of 7.23 mW in rms in measurements (with a matching resistive load 1.4 kΩ) at 10 000 r/min of the rotor speed.

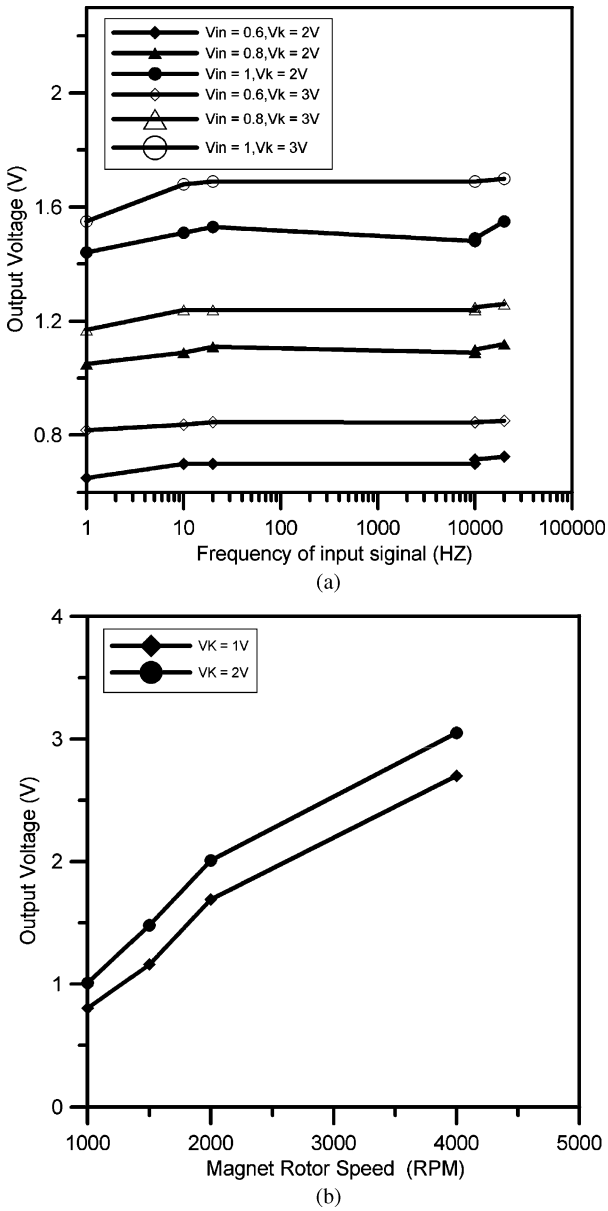

Fig. 9. Measured output voltage of the designed circuit versus (a) input frequency with fixed amplitude; (b) rotor r/min.

The fabricated energy harvest circuit is next utilized to collect the energy to the output capacitor, where the switchings of the diode-connected transistors are implemented by an 8051 microprocessor. In the future, these switchings will be implemented by a very low-power digital circuit. Fig. 9(a) shows the measured output voltage for the input signal from 1 to 10 kHz, while Fig. 9(b) shows those with magnet rotor speed from 1 to 4 K r/min. It is seen from Fig. 9(a) that with V_b ranging from 2 to 3 V for different input ac voltages, the circuit successfully outputs varied dc voltage level for different input ac frequencies, but with a fixed ac amplitude. However, due to the two previously mentioned reasons (possible misassignment of V_b and

$\{C_1, \ldots, C_4\}$, and delayed switchings on the transistors) the steady-state output voltages fall well below the expected output voltage given in (11), the quadruple of the amplitude of the input ac signal in Fig. 9(a). In result, the efficiency of the harvest circuit does not achieve its optimum capability. One can measure the efficiency of the harvest circuit by simply calculating $P_{\rm out}/P_{\rm in}$, where $P_{\rm in}$ is the measured output power of the microgenerator, while the later $P_{\rm out}$ can be measured again by connecting a resistance load to the output node of the harvest circuit. For the case with $V_{\rm in} = 0.6$ V (output voltage in peak-to-peak by the microgenerator), the input current 20 uA, the load resistance 610 kΩ and $V_b = 2$ V in Fig. 9(a), based on measurement, the efficiency is about 2.492 uW/9.05 uW = 27.53%. Note that without the proposed diode-connected MOS transistors with capacitors across gates and drains, the input signals would not be able to overcome the threshold of $\{M5, \ldots, M8\}$ to generate any nonzero output power. Finally, it is seen from Fig. 9(b) that the output voltage increases with an increasing rotating speed of the microgenerator for two different charging biases. It is because of an increasing ac output amplitude while the rotor speed is increased.

VII. Conclusion

A self-powered microenergy harvester comprising a CMOS energy-harvest IC and an external miniaturized rotary generator has been designed, fabricated, and tested. A miniaturized rotary generator with an eight-pole magnet rotor and planar coils are presented in this study. The whole volume is approximately $10 \times 10 \times 2$ mm^3. The theoretical analysis and finite-element modeling are successfully performed to predict the nonuniform magnetic field distribution over the coils, which is set up for later GA optimization. Optimization found that the coils should not fully fill available sectoral space to render the maximum power. It is due to the fact that long coils lead to large resistance and then decreasing the power. With hardware of the microgenerator successfully designed and fabricated, a novel energy circuit employing Dickson charge pump with diode-connected MOS transistors is designed and fabricated. Experimental results clearly show that the circuit is capable of collecting ac power into the form of a dc voltage across an output capacitor.

In the future, an adjustable gap between the microcoil and magnet will be designed, and different size coils and magnets will be studied and discussed. As for the energy-harvest circuit, the optimum values V_b and $\{C_1, \ldots, C_4\}$ should be solved and used for the best output voltage, the quadruple of the amplitude of the input ac signal. Also, effects of delayed switchings on the transistors ought to be studied. Finally, it is noted at this stage that the generator developed in this study requires an input electric power to rotate the rotor in order to generate power. In the future, this generator could be integrated with a bicycle to generate power for a light-emitting diode (LED) as lighting or as a warning sign for security, and with a car as a power source for tire pressure monitoring.

Acknowledgment

This work was supported by the National Science Council of ROC through Contracts NSC97-2221-E-009-057-MY3 and NSC97-2220-E-009-029. the authors would like to thank the National Chip Implementation Center (CIC) of Taiwan for providing the 0.35-um mixed-signal CMOS process.

References

[1] P. Glynne-Jones and N. M. White, "Self-powered systems: A review of energy sources," *J. Sensor Rev.*, vol. 21, no. 2, pp. 91–97, 2001.

[2] S. Roundy, "Toward self-tuning adaptive vibration based micro-generators," in *Proc. SPIE Int. Symp. Smart Mater. Nano and Micro-Smart Syst.*, 2004, pp. 373–384.

[3] C. W. Chiu and P. C.-P. Chao, Industrial Technology Research Institute (ITRI) of Taiwan Tech. Rep., Dec. 2003.

[4] B. Otis and J. Rabaey, "A 300_W 1.9 GHz oscillator utilizing micromachined resonators," *IEEE J. Solid State Circuits*, vol. 38, no. 7, pp. 1271–1274, Jul. 2003.

[5] S. Roundy, P. K. Wright, and J. Rabaey, *Energy Scavenging for Wireless Sensor Networks With Special Focus on Vibrations*. Norwell, MA: Kluwer, 2003.

[6] C. T. Pan and T. T. Wu, "Development of a rotary electromagnetic microgenerator," *J. Micromech. Microeng.*, vol. 17, p. 120, 2007.

[7] S. Das, D. P. Arnold, I. Zana, J. W. Park, J. H. Lang, and M. G. Allen, "Multi-watt electric power form a microfabricated permanent-magnet generator," in *Tech. Dig. 18th IEEE Int. Conf. Micro Electro Mech. Syst.*, 2005, pp. 278–290.

[8] D. P. Arnold, F. Herrault, I. Zana, P. Galle, J. W. Park, S. Das, J. H. Lang, and M. G. Allen, "Design optimization of an 8-Watt, microscale, axial-flux, permanent-magnet generator," *J. Micromech. Microeng.*, vol. 16, pp. S290–S296, 2006.

[9] S. Das, D. P. Arnold, I. Zana, J.-W. Park, M. G. Allen, and J. H. Lang, "Microfabricated high-speed axial-flux multiwatt permanent-magnet generators—Part I: Modeling," *J. Microelectromech. Syst.*, vol. 15, no. 5, pp. 1330–1350, Oct. 2006.

[10] D. P. Arnold, S. Das, J.-W. Park, I. Zana, J. H. Lang, and M. G. Allen, "Microfabricated high-speed axial-flux multiwatt permanent-magnet generators—Part II: Design, fabrication, and testing," *J. Microelectromech. Syst.*, vol. 15, no. 5, pp. 1351–1363, Oct. 2006.

[11] A. S. Holmes, G. D. Hong, and K. R. Pullen, "Axial-flux permanent magnet machines for micropower generation," *J. Microelectromech. Syst.*, vol. 14, pp. 54–62, 2005.

[12] H. Raisigel, "Magnetic planar micro generator," in *Proc. 12th Int. Conf. Solid-State Sens. Actuators Microsyst.*, 2005, vol. 2, pp. 757–761.

[13] H. Raisigel, O. Cugat, and J. Delamare, "Permanent magnet planar microgenerators," *Sensors Actuators A*, vol. 130-131, pp. 438–444, 2006.

[14] J. Dickson, "On-chip high-voltage generation in NMOS integrated circuits using an improved voltage multiplier technique," *IEEE J. Solid-State Circuits*, vol. 11, no. 3, pp. 374–378, Jun. 1976.

[15] T. Tanzawa and T. Tanaka, "A dynamic analysis of the Dickson charge pump," *IEEE J. Solid-State Circuits*, vol. 32, pp. 1231–1240, Aug. 1997.

[16] J. A. Starzyk, Y.-W. Jan, and F. Qiu, "A DC-DC charge pump design based on voltage doublers," *IEEE Trans. Circuits Syst. I, Fund. Theory Appl.*, vol. 48, no. 3, pp. 350–359, Mar. 2001.

[17] M. Mitchell, *An Introduction to Genetic Algorithms*. Cambridge, MA: MIT Press, 1998.